Received: 28 July 2023 | Revised: 28 November 2023 | Accepted: 29 November 2023

DOI: 10.1002/hyp.15053

RESEARCH ARTICLE

WILEY

Impact of solar panels on runoff generation process

Giorgio Baiamonte | Luciano Gristina | Samuel Palermo

Department of Agricultural, Food and Forest Sciences, University of Palermo, Palermo, Italy

Correspondence
Giorgio Baiamonte, Department of Agricultural, Food and Forest Sciences, University of Palermo, viale delle Scienze 13, 90128 Palermo, Italy.
Email: giorgio.baiamonte@unipa.it

Abstract

Because of the benefits of solar energy, solar photovoltaic (PV) technology is being deployed at an unprecedented rate and the number of photovoltaic panels is sharply increasing. Agrophotovoltaic systems (solar farms) seem to be the most sustainable tools to create renewable energy without compromising agricultural production. However, utility-scale solar energy development is land intensive and its large-scale installation can have negative impacts on the environment. Moreover, its impacts on soil and on relative hydrological processes have been poorly studied. This article aims to evaluate the impact of solar panels on the runoff generation process, which is directly linked to the soil erosion process. Using a rainfall simulator, runoff measurements for a rainfall intensity equal to 56 mm/h were carried out by assuming different panel arrangements with respect to the maximum slope direction of the field (cross slope and aligned slope). Results were compared to a control reference of the same plot, with no panels (bare soil). Physical models found in the literature were then applied and calibrated, to upscale the models to a much higher hillslope length. Results showed that solar panels increase the peak discharge by about 11 times compared to the reference hillslope. A moderate effect of PV panel arrangement was observed on the peak discharges (11.7 and 11.5 times higher, for cross slope and aligned slope panels, respectively), whereas the time to runoff was the lowest for aligned slope panels (0.3 h), higher for cross slope panels (0.62 h), and the highest (1.2 h), for the bare soil hillslope. As it would be expected, upscaling the models to longer hillslopes resulted in increases in outlet discharges, and in the time to runoff, with an exception for aligned slope panels.

KEYWORDS
border irrigation, experimental measurement, infiltration model, kinematic wave model, rainfall simulator, runoff generation, solar panels

1 | INTRODUCTION

The need for climate change mitigation, energy security improvement, and sustainable human activities is driving a rapid transition from carbon fuels to renewable energy (IPCC, 2014). Solar energy is one of the renewable energy systems with the greatest climate change mitigation potentials with life cycle emissions as low as 14 g CO_2-eq·kW·h^{-1}, compared to 608 g CO_2-eq·kW·h^{-1} for natural gas (Hernandez et al., 2014).

At the global level, several analyses have shown that photovoltaic (PV) power systems could grow almost sixfold over the next 10 years, reaching a cumulative capacity of 2840 GW globally by 2030 and

rising to 8519 GW by 2050, resulting in a total expected installed capacity almost 18 times higher than that of 2018. Around 60% of the total PV capacity in 2050 would be produced by solar farms at the utility-scale, while the remaining 40% would be distributed individually (rooftop system) (IRENA, 2019). In Italy, the creation of photovoltaic fields installed on the ground are one cause of reversible soil consumption currently covering more than 17 500 hectares of land.

The Integrated National Energy and Climate Plan (PNIEC, 2023) aims to instal 52 GW of PV systems by 2030, However, considering the 22 GW installed by 2020, an additional 30 GW are necessary. Thus, over additional 50 000 ha of land will be necessary to reach the national plan's target.

Such a large land use change due to the expected increase in PV systems in the next future must be weighed against the strong trade-off made with agricultural land (Dupraz et al., 2011), and the subsequent landscape impact caused by the installation of the panels. In fact, it seems necessary to investigate approaches aimed at making the spread of the PV panels compatible with the natural landscape as well as with agricultural production. Specifically, the visual impact of photovoltaic parks, caused by the large area covered by the panels, and the consequences of their installation on soil fertility and, in the long term, land value (Bignami, 2010) must be considered.

These considerations are confirmed by important changes regarding the application of photovoltaics in agriculture contained in the legislative decree transposing directive 2009/28/EC, approved by the Council of Ministers on 3 March 2011. Article 8 of this decree contains specific provisions aiming to place a limit on the subtraction of agricultural land, an issue brought up on several occasions by trade associations.

Low income from farming has encouraged agricultural entrepreneurs to replace agricultural activity with photovoltaic systems, leading to large-scale land-use changes and subsequent trade-offs. Recently economic incentives have aimed to combine renewable energy production needs with agricultural activity to improve environmental safeguards. This policy direction suggests further development, expansion, and opportunities for PV systems.

Several studies have been conducted on the technology of PV systems, and on the effect that they have on-farm productivity and ecosystem modification (Wu et al., 2022; Zainol Abidin et al., 2021), often due to non-uniform water distribution on the ground and changes in soil quality. The latter because the solar panels located above the cultivated soil have an unexplored effect on rain redistribution, protecting large parts of the soil but also concentrating flows on a limited part of it (Elamri et al., 2018).

From the soil quality point of view, physical, chemical, and overall soil quality indexes are more altered under solar panels than in open fields (Lambert et al., 2021) mainly due to solar park construction altering soil structure and as well as soil physical characteristics.

On the contrary, few studies have been carried out on the impact that PV systems have on the runoff generation process and on soil erosion (Choi et al., 2020; Elamri et al., 2018). These studies have only focused on the spatial patterns of rain redistribution on the ground, between panels and bare soil. They have also shown the strong differences in rain drop size distribution and consequently in rain kinetic energy and have investigated and modelled runoff velocity (Cook & McCuen, 2013).

Cook and McCuen (2013) also studied the potential soil erosion at the base of solar panels, identifying evident high detachment processes caused by the high intensity and kinetic energy of the discharge flowing off the panels as well as high transport processes and rill erosion phenomena. However, no quantitative information was given about the impact of solar panels on the runoff generation process causing soil erosion.

In consideration of the above, the objective of this article is to investigate the impact of solar panels on the runoff generation process from both an experimental and theoretical point of view. The effect of the different orientations of solar panels with respect to the maximum slope direction of the PV system site is also analysed. Finally, physical models provided by the literature that help explain the impact of solar panels on runoff generation have been calibrated for the experimental layouts, so that the same models could be upscaled to different hillslope length values.

2 | MATERIALS AND METHODS

2.1 | Description of the experimental layout

The experimental measurements were carried out at Santa Margherita Belice (Agrigento, Sicily), at the coordinates 37°41′43.04″ N, 13°02′49.14″ E. To investigate the influence of solar panels on runoff generation, a 'bare soil' hillslope (layout A) was considered as a useful control reference (Figure 1a). The solar panels were installed on the same hillslope later. To also investigate the effect of solar panels' orientation with respect to the maximum slope direction, two different panel arrangements were selected (Figure 1b,c). In particular, layout B) (cross slope) regards the case in which the panels' slopes cross that of the hillslope, thus their slope is perpendicular to the maximum slope direction of the hillslope (Figure 1b). In layout C (aligned slope), the slope of two panels is along that of the hillslope, and the discharge flowing off from the upstream (US) panel provides an additional contribution to the downstream (DS) panel (Figure 1c). The cross slope panel case accounts for east–west exposition, whereas the aligned slope case accounts for north–south exposition.

The experimental plot was wide $B = 1$ m and long $L = 3$ m with a slope $S_0 = 14\%$. it was hydraulically separated along the plot boundary and a Gerlach apparatus was installed at the outlet for runoff measurements. Figure 2a illustrates the experimental layout corresponding to layout B (cross slope panels, Figure 1b), including the rainfall simulator and Gerlach apparatus, while Figure 2b shows layout C (aligned slope, Figure 1c).

Generally, solar panels can come in several sizes. In the present investigation, the selected panel size was $L_p = 0.8$ m (length) and $B_p = 1$ m (width B equal to that of the plot, Figure 1c). Their were spaced 0.3 m apart for cross slope panels, and 0.7 m apart for aligned slope panels.

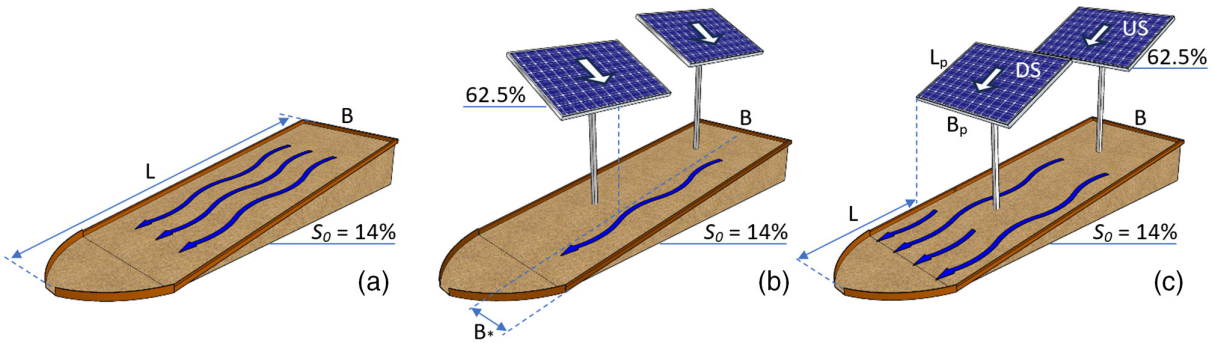

FIGURE 1 Schematic representation of the experimental setup: (a) bare soil (a), (b) cross slope panels (b), and (c) aligned slope panels (c).

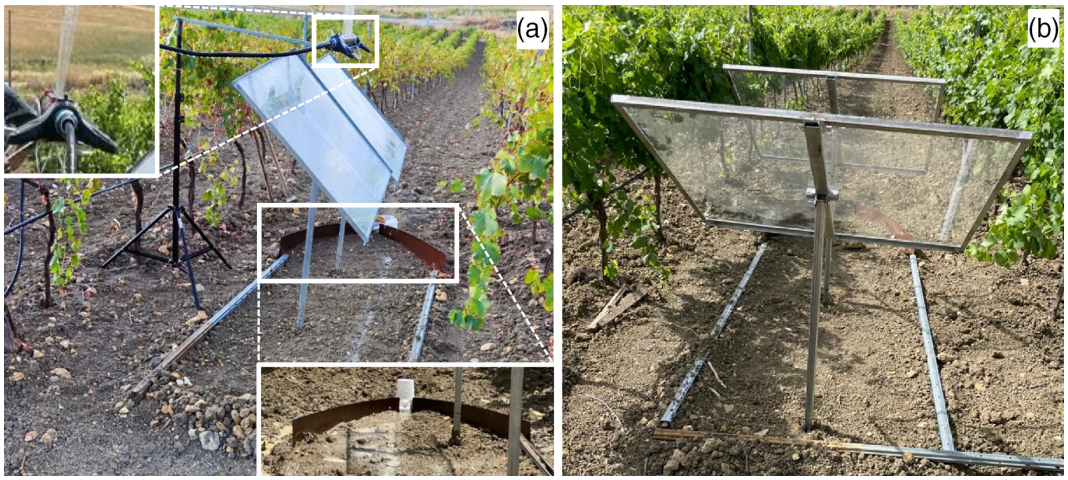

FIGURE 2 Images illustrating (a) the layout B (cross slope panels, Figure 1b), and (b) the layout C (aligned slope panels, Figure 1c). In Figure 2a), the rainfall simulator and the Gerlach apparatus are also zoomed in.

Panels were built by using glass plates on a tilting metal support that can be adjusted according to the correct angle with respect to the sun (Figure 2b). The angle was set to 62.5% for both cross and aligned slope panels in correspondence with the commonly applied angle over the horizon (32°). The height from the ground was the same as in reality (1 m).

An automated sprinkler (Figure 2a) that runs in cycles was used to simulate rainfall. One cycle takes 11 s and consists of the sprinkler boom moving back and forth once. During cycles, the rainfall simulator applied rainfall over the entire the area of interest.

The average applied rainfall during one cycle (cycle rainfall load) was determined by calibration with rain gauges. Thus, before performing runoff measurements, the spatial distribution of rainfall intensity simulated by the rainfall simulator illustrated in Figure 2a was analysed.

A grid of 7 × 24 (168) catch cans were arranged on the bare plot (Figure 1a) to collect the rainfall depth during a simulated rainfall of 240 min and the rainfall intensity was calculated in each point. Figure 3 shows the empirical distribution of rainfall intensity together with the fitted normal distribution corresponding to the mean, $\mu = 56.04$ mm/h, and to the standard deviation, $\sigma = 7.93$ mm/h. The coefficient of variation was CV = 14.1%. The corresponding Christiansen uniformity coefficient was equal to UC = 89%, making the simulated rainfall uniform enough for the purpose of this study. Also, due to the satisfactory goodness of fit of the normal distribution, the mean value $i = 56$ mm/h (Figure 3) was considered as a representative value of the simulated rainfall for the entire plot, and it was imposed as a constant during experimental runs for the three layouts.

Of course, for layouts B and C the solar panels strongly altered the water application uniformity on the plot due to the concentration of runoff off from the panels at their outlets. To have an idea of how much the applied water volume characteristics changed when hitting the soil without and with panels, Figure 4 shows a comparison of the water granulometry patterns. The different patterns were detected by using the flour pellet method (Kincaid et al., 1996; Kohl, 1974), without panels (Figure 4a) and at the outlet of the panels (Figure 4b). As expected the drop size distribution of the simulated rainfall was significantly altered when the water hitting the soil was concentrated at the panels' outlet (Cook & McCuen, 2013).

This issue may be important for the overland flow process analysed in this study, but it would be much more relevant in the context of soil erosion, since the energy associated with the water application

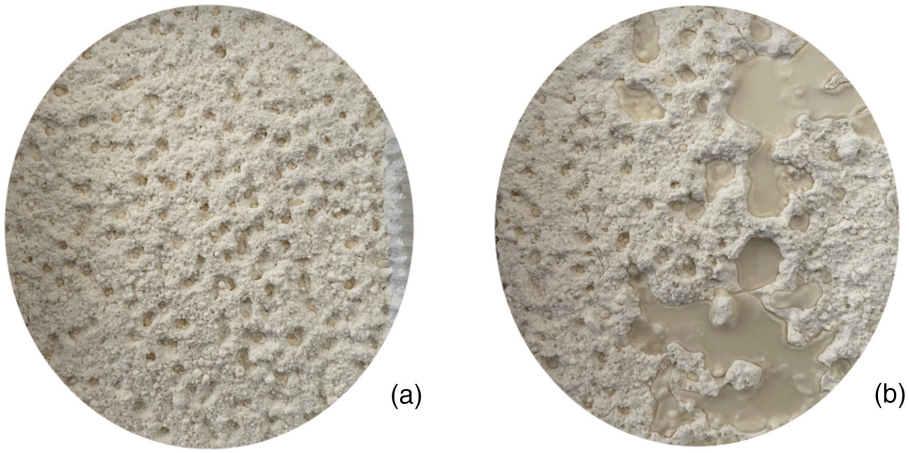

FIGURE 3 Empirical distribution of rainfall intensity measured by 7 × 24 (168) catch cans arranged on the bare plot (Figure 1a). The red line indicates the fitted normal distribution ($\mu = 56.04$ mm/h, blue dot; $\sigma = 7.93$ mm/h; CV = 14.1%).

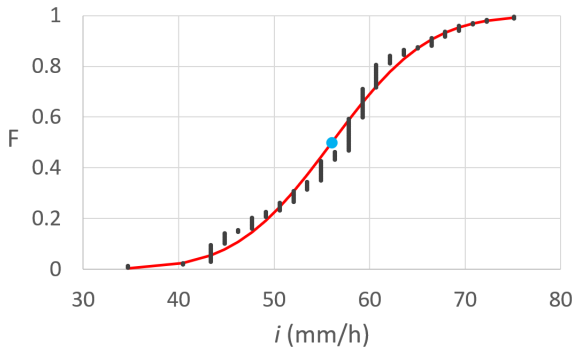

FIGURE 4 Flour cup exposed to a rainfall with intensity $i = 56$ mm/h (a) under open ground, and (b) under the solar panel outlet.

rate when there are no panels would be expected to be much less than that when the panels are present.

The runoff samples were collected in 1-L bottles every 5 min. The time to fill the runoff bottle was recorded. After each run, the sample bottles were immediately weighed to determine the runoff volume. The bottles were subsequently incubated in an oven at 105°C for at least 24 h or until the sediments were dried. The dry weights were then recorded to calculate the sediment delivery, and thus to correct the surface runoff calculation.

2.2 | Applying simplified overland flow models

For layout A (bare soil), an already available simplified overland flow model (GA-KW model, Baiamonte & Agnese, 2010) was applied that combines the Green and Ampt model (Green & Ampt, 1911), to account for infiltration, and the 1D kinematic wave model (Woolhiser & Liggett, 1967), to account for the transportation process along the hillslope.

The GA-KW model is shortly summarized in Appendix A and can be directly applied to layout A (bare hillslope), under the assumption that the plot is perfectly planar, and thus the flow is rigorously downslope and the unsteady and spatially varied overland generation occurs as a sheet flow that entirely covers the hillslope. Rainfall (minus infiltration losses) constitutes the lateral inflow to the plane.

Under a constant rainfall intensity of i (mm/h), Baiamonte and Agnese (2010) derived the characteristic curves corresponding to three domains of the kinematic plane (the first two for the rising limb of the hydrograph, and the third for the falling limb), depending on parameters related to rainfall, hillslope geometry, and soil. The singularity of such a solution is its ability to account for the decreasing of the infiltration capacity, f (mm/h), during the runoff generation process, that in turn determines an increase in the rainfall excess intensity, $r = i - f$. For the case of an impervious hillslope, Baiamonte and Agnese (2010) also showed that their solution agrees with the kinematic wave model originally introduced by Woolhiser and Liggett (1967).

In the following, only the parameters referring to the soils and to the hillslope which were calculated for the experimental layouts, and minor model description, are reported. For model details, the reader can refer to Baiamonte and Agnese (2010) or to Appendix A.

According to Green and Ampt (1911), overland flow generation starts when rainfall intensity exceeds the soil infiltration capacity and the time to ponding, t_p, is reached (Baiamonte, 2016). The time to ponding, τ_p, normalized with respect the sorptivity time scale, t_c, is written here:

$$\tau_p = \frac{t_p}{t_c} = \frac{1}{\rho(\rho - 1)}, \quad (1)$$

where ρ is the ratio between the rainfall intensity, i (mm/h), and saturated hydraulic conductivity, K_s (mm/h), whereas the sorptivity time scale t_c (h) reads:

$$t_c = \frac{(\theta_s - \theta_0)\,\psi_m}{K_s} = \frac{\omega}{K_s}, \quad (2)$$

where θ_s (cm^3 cm^{-3}) and θ_0 (cm^3 cm^{-3}) are the volumetric water contents corresponding to the saturated and antecedent soil moisture conditions, respectively, and ψ_m (mm) is the matric potential at the

wetting front. In Equation (2), the temporal scale t_c, was also written by consolidating the soil hydrological characteristics θ_s, θ_0 and ψ_m in the ω (h) parameter, which will be calibrated later.

Regarding the hillslope geometry, the following hillslope 'geometry' parameter, k_*, needs to be determined (see Appendix A):

$$k_* = \frac{3.6\sqrt{S_0}}{n_{\text{Mann}} L}, \tag{3}$$

where S_0 is the slope, and 3.6 is a conversion factor that lets the length of the hillslope, L, be expressed in (m), the Manning friction factor, n_{Mann}, be expressed in ($m^{-1/3}$ s), and the specific discharge, q, be expressed in (mm/h).

In the GA-KW model, a dimensionless parameter, $\tau_{\text{eq,i}}$, introduced later (Baiamonte & Singh, 2016), synthesizes both the hillslope geometry and the soil hydrological characteristics, that is, the ratio between $t_{\text{eq,i}}/t_c$, with $t_{\text{eq,i}} = 1/\sqrt{k_*}\, i$ that only depends on the rainfall intensity and on the hillslope geometry:

$$\tau_{\text{eq,i}} = \frac{1}{t_c\sqrt{k_* i}} = \frac{K_s}{\omega}\sqrt{\frac{n_{\text{Mann}} L}{i\sqrt{S_0}}}. \tag{4}$$

This parameter denotes the time to equilibrium corresponding to an impervious hillslope, $t_{\text{eq,i}}$, normalized with respect to the sorptivity temporal scale, t_c. The soil (t_c) is the scale factor and plays an important role in simulating the overland flow process on an infiltrating hillslope.

The separation of the 1st and 2nd domain ($t < t_k$ or $t > t_k$, respectively) of the kinematic plane depends on the normalized kinematic wave arrival time, t_k, associated with the corresponding infiltration capacity, f_k (Baiamonte & Singh, 2016). The time t_k represents the time that an observer (the runoff), starting from the top of the hillslope, takes to reach the bottom (during the infiltration process). If the duration of rainfall, t_r, is less than t_k, the recession starts before the observer has achieved the bottom of the hillslope, whereas if $t_r > t_k$, the raising limb of the hillslope continues because of the decreasing infiltration capacity as described by the Green-Ampt model. Of course, the falling limb occurs for $t > t_r$ (3rd domain).

The relationships of t_k and f_k are reported here, respectively, in a more compacted dimensionless form that was derived in Baiamonte and Singh (2016):

$$\tau_k = \frac{t_k}{t_c} = \tau_p + \frac{\rho^{-1}}{(f_{*k}-\rho^{-1})} - \frac{\rho^{-1}}{(1-\rho^{-1})} + \psi_k \text{ with } \psi_k = ln\left(\frac{f_{*k}-\rho^{-1}}{f_{*k}(1-\rho^{-1})}\right), \tag{5a}$$

$$f_{*k} = \frac{f_k}{i} = 1 - \frac{(1-\rho^{-1})(f_{*k}-\rho^{-1})^2}{(f_{*k}+1-2\rho^{-1})\rho^{-2}}\left(\tau_{\text{eq,i}}^2 - \frac{2\rho^{-1}\psi_k}{f_{*k}-\rho^{-1}} - \psi_k^2\right), \tag{5b}$$

where $\tau_{eq,i}$ is expressed by Equation (4).

For the layout B (cross slope panels), the overland flow model considered for the layout A can also be applied. Indeed, for cross slope panels, a uniform water application rate, flowing out from the panels, is assumed to be uniformly applied over the hillslope characterized by a width B_* less than that of the layout A (see Figure 1b). Thus, the reduced hillslope is also assumed to be perfectly planar for layout B, and the flow is rigorously downslope, whereas the lateral in flow is represented by the discharge flowing off from the panels along the perpendicular direction with respect to the slope of the hillslope. In such a condition, all the runoff water particles move linearly downslope, so that no water passes under the solar panel (see Figure 1b).

One more assumption is introduced: that the equilibrium between the rainfall intensity, i(mm/h), and the outlet panel specific discharge, q(mm/h), is instantaneous ($q = i$), which is not far from the actual conditions since the length of the panels is usually very small, compared to the length of the hillslope characterized by a slope S_0 that is much less than that of the solar panels (62.5%).

For layouts C (aligned slope), the overland flow model considered for layouts A and B cannot be applied, since the assumption of a uniform water application rate, which is at the base of the GA-KW model, is far from being appropriate. This is because the water application rate generated over the upstream panel (US) concentrates at the panel bottom, and later interacts with that of the downstream panel (DS) where, similarly to the US panel, the discharge outflowing from the panel is generated. Thus, contrarily to the situation in cross slope panels, where it is assumed that no water passes under the solar panels, on aligned slope panels, all the runoff water particles move linearly downslope, so that their outflows interact. Therefore, for this layout the area right under the DS solar panel is subject to infiltration (Figure 1c).

Layout C can also be addressed by likening it to border irrigation, where a similar runoff generation process can be recognized. Indeed, in border irrigation, water is introduced at the upstream end of the hillslope (at the bottom of each panel in our case) and is allowed to move as a sheet flow which covers the entire width of the border in the downstream direction (Singh & Su, 2022). It should be noted that if we have a matrix of aligned slope panels on a hillslope, there would be a contribution from the space between panels flowing downward, which in this study did not occur (with panel width being equal to the hillslope width).

A simplified mathematical model for border irrigation was introduced by Singh and Yu (1987). The model is described in two companion articles. In the first article (Singh & Yu, 1987), the advance and storage phases are developed, while the second article accounts for the vertical and horizontal recession phases. For the purpose of this work, which aims to investigate the impact of solar panels on the alteration of peak discharge, only the advance and storage phases leading to the rising limb of the hydrograph were considered.

Singh and Yu (1987) used the volume balance approach and calibrated their model by experimental data from vegetated and nonvegetated borders (Atchison, 1973; Roth, 1971). Average errors were found very limited, making their approach suitable to be applied. In the following, only a brief description of the border irrigation model

and of its parameters will be given, and for further details the reader may refer to Singh and Yu (1987).

For the advance and storage phases, the model parameters are (i) Kostyakov's empirical infiltration parameter, K (m/min^A) (Kostyakov, 1932), (ii) Kostyakov's time exponent, A, (iii) Manning's roughness factor, n_{Mann} (min m$^{1/3}$), iv) distance, L_{av}, at which the average surface water depth, h_{av}, between $x = 0$ and advance front $x = S$, reaches 95% of the normal water depth h_0, and v) the entrance normal flow depth coefficient, α.

Although the parameters L_{av} and α are related to many factors such as infiltration rate, slope and surface roughness, Singh and Yu (1987) verified that L_{av} and α are slightly related to these factors, compared to the other parameters of the model, thus they were assumed to be constant, as suggested by Singh and Yu (1987). In particular, $L_{av} = 75$ m for a nonvegetated border, $L_{av} = 225$ m for a vegetated border, and $\alpha = 0.620$ for both a vegetated and nonvegetated border.

The advance front reaches the end of the border ($x = L$) at $t = T_a$ (min), and the inflow continues until the cut off time, t_r. After the time T_a, the storage phase begins to develop, where the water depth variation from upstream (normal water depth, h_0, corresponding to the Manning equation) to downstream (h_e) is assumed to be linear. Singh and Yu (1987) derived the temporal variation of water depth at the downstream end, h_e:

$$h_e = \left[\frac{n_{Mann}}{60\sqrt{S_0}}\left(q_0 - \frac{KL}{T_a}\left(t^A - (t - T_a)^A\right)\right)\right]^{0.6}, \quad (6)$$

where the factor 60 makes it possible to express n_{Mann} in (m$^{-1/3}$ s), S_0 is the slope, and q_0 (m^3/m/min) is the unit width inflow rate that, maintaining the assumption of instantaneous equilibrium at the bottom of each panel, can be related to the rainfall intensity i and to the panel length L_p, with surface area $S = B_p \times L_p$ (Figure 1c):

$$q_0 = \frac{i L_p}{60 \times 1000}, \quad (7)$$

where 60×1000 lets q_0 be expressed in (L/h/m), and i in mm/h. In Equation (6), the term in round brackets is the net outflow discharge, Q, of interest, which accounts for the infiltration during the storage phase, and it is rewritten here to express Q and i in (L/h/m), L in (m), K in (mm/h^A), n_{Mann} in (m$^{-1/3}$ s) and t and T_a in hours:

$$Q = i L_p - \frac{KL}{60^{1-A} T_a}\left(t^A - (t - T_a)^A\right). \quad (8)$$

Equation (8) can be applied to determine the outlet discharge that depends on the distance L from the edge of the panel to the outlet (Figure 1c), from the time that the advance front reaches the outlet, T_a (h), and of course from Kostyakov's infiltration parameters, K and A.

Equation (8) can also be rewritten to express the specific outflow discharge, q (mm/h), that is, the discharge Q per unit surface area $(L_p + L)\,B$, which is useful to consider to obtain the quasi-equilibrium condition (i.e., when $q \cong i - K_s$):

$$q = \frac{i B L_p T_a - 60^{A-1} K L\left(t^A - (t - T_a)^A\right)}{B(L_p + L) T_a}. \quad (9)$$

Of course, for $t = T_a$, when the advance front reaches the end of the border, the outflow matches the inflow rate i minus the infiltration rate according to Kostyakov's equation:

$$q = \frac{i B L_p - 60^{A-1} K L}{B(L_p + L)}. \quad (10)$$

where q is in mm/h.

3 | RESULTS

3.1 | Experimental measurements

For layouts A–C, Figure 5 plots the output's specific discharge, q (mm/h), versus the time, for the two replications performed for each layout. Figure 5 shows that runoff measurements were carried out mostly for the rising limb of the hydrograph. This is because the purpose of this work is to investigate the impact of solar panels on the alteration of peak discharge at the end of the rising limb. Thus, measurements for the recession of the hydrograph, after the rainfall ceased, were only carried out for a few cases of the second replication (run #2, Figure 5a,b).

Although the hillslope was regularized before performing the measurements, and the latter were carried out after a long dry period with neither rainfall nor irrigation, two replications exhibited quite dispersed measurements. This can be ascribed to the following reasons: (i) the antecedent moisture conditions, (ii) the spatial variability of the soil's hydrological characteristics and of the field microtopography, (iii) the rainfall uniformity and (iv) the experimental error. In particular, microtopography can govern runoff dynamics as a net result of local heterogeneities in the flow paths and ponding (Baiamonte et al., 2014). This in turn controls the development of the surface water layer that connects and flows downslope (Caviedes-Voullième et al., 2021; McDonnell et al., 2021).

However, considering the complexity of the studied process, measurements were judged to be accurate enough to be analysed, especially for layouts A and B. The highest peak discharge of Figure 5a, occurring for the first replication (run #1) could be caused by occasional soil bumps that disturbed the overland flow, which were not contemplated in the physical model. On the other hand, Figure 5c clearly shows a drop in discharge in both replications determined by the aligned slope panels, making evident the time in which the contribution of the US panel reaches the outlet, quickly increasing the discharge flowing out the DS panel. The maximum specific discharge can be observed for layout B) (cross slope panels, Figure 5b).

It is important to note that for the three layouts, the rainfall duration was enough to achieve the equilibrium condition, which is useful for the models' calibration. Moreover, a comparison of Figure 5a–c

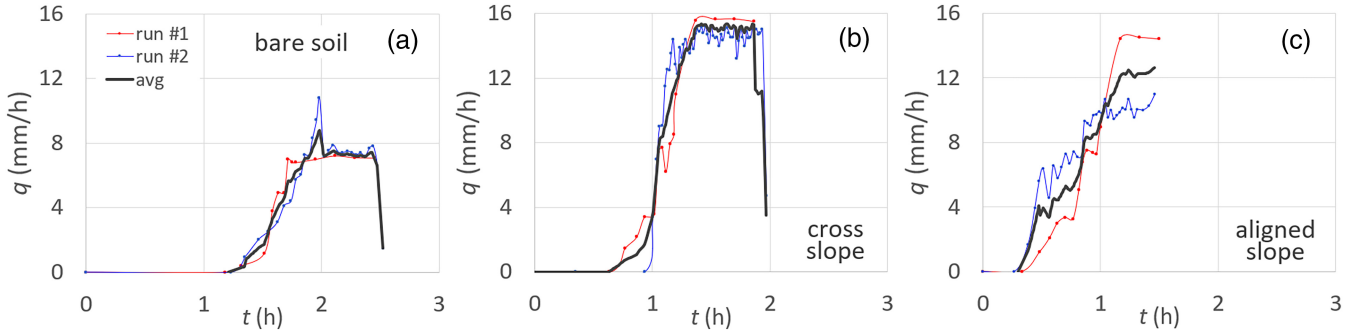

FIGURE 5 Temporal variations of specific discharge measurements performed with two replicates and their average (avg), corresponding to (a) layout A (bare soil), (b) layout B (cross slope panels) and (c) layout C (aligned slope panels) (Figure 1).

TABLE 1 Input parameters corresponding to Layouts A and B.

Layout	Model	i (mm/h)	K_s (mm/h)	ρ	t_c (h)	t_r (h)	L (m)	n_{Mann} (s m$^{-1/3}$)	S_0 (%)	k_* (equation (3))
(A) bare soil	GA-KW	56	**39.2**	1.38	**0.484**	2.47	3	**0.909**	0.14	0.4939
(B) cross slope panels		**62.1***		1.58		1.87				

Note: *Indicates that the amplified rainfall intensity. Bold values indicate calibrated parameters.

shows that runoff generation is quicker when panels are arranged aligned with the hillslope (0.3 h) (Wang & Gao, 2023) (Figure 5c) rather than arranged cross slope (0.62 h) (Figure 5b), and that the lowest and the most delayed response occurred for bare soil (1.2) (Figure 5a). The latter is probably due to the delay effect induced by the infiltration process being much more pronounced than when panels lay on the hillslope. The times to runoff generated by the calibrated models were very close to those observed.

For the three layouts, Figure 5 also plots the average value of the two replications (avg, black lines) that will be considered for the models' calibration, as discussed in the next section.

3.2 | Calibrating the overland flow models

For layout A (bare soil), Table 1 reports the input parameters required by the overland flow GA-KW model (Baiamonte & Agnese, 2010). Note that only the rainfall intensity, i (mm/h), the slope, S_0, and the length of the hillslope, L (m), were strictly considered as input parameters, while the saturated hydraulic conductivity, K_s (mm/h), the sorptivity time scale, t_c (h), and the Manning coefficient, n_{Mann} (s m$^{-1/3}$), are parameters that need to be calibrated according to the runoff measurements. Indeed, for layout A, by combining Equation (1) and Equation (2), the observed time to ponding, t_p, and the specific discharge at the equilibrium ($i - K_s$) makes it possible to derive both the saturated hydraulic conductivity, K_s, and the ω (h) parameter, which is related to the sorptivity time scale, t_c, and consolidates the role of ψ_m, θ_s and θ_0 (Equation (2)). The n_{Mann} parameter was calibrated by minimizing the mean square errors between the measured and estimated specific discharges. In Table 1, the values of the calibrated parameters are indicated in bold. Note that the calibration of n_{Mann} provides a high value equal to 0.909 s m$^{-1/3}$. This occurrence could be ascribed to the marginally/partially inundated flow regime (Lawrence, 1997) characterizing the experimental conditions. Indeed, for the low water depths provided by the model (2–4 mm), the macroscale surface roughness may determine high frictional resistance in overland flow. Experimental measurements of Abrahams and Parsons (1994) and of Roels (1984) showed that in such a particular condition, where the inundation ratio (i.e., the ratio of the mean flow depth to the average roughness height) is close to the unity, the Darcy–Weisbach friction factor may reach 20–30, and for water depths 2–4 mm, these values correspond to Manning coefficients equal to 0.803–1.192 s m$^{-1/3}$, and to 0.819–1.196 s m$^{-1/3}$, respectively, justifying our finding.

As previously observed, for layout B, the GA-KW model was also applied since it was assumed that the discharge outflowing from the panels was uniformly applied to the hillslope (Figure 1b). The parameters calibrated for layout A were also imposed for layout B), since it was assumed that the soil's hydrological characteristics and the hillslope roughness did not significantly differ from those of layout A (bare soil). However, because of the different panels' orientation, the hillslope width was reduced by replacing B by B_* (Figure 1b). Since the GA-KW model was applied in terms of the specific discharge, q (mm/h), it was enough to amplify the rainfall intensity by considering the reduced width B_*. The B_* value, and the associated amplified rainfall intensity, was calibrated by once again minimizing the mean square errors between the measured and estimated specific discharges. Thus, an amplified rainfall intensity of 62.1 mm/h was obtained (Table 1).

For layouts A and B, the results obtained by the calibrated GA-KW model are illustrated in Figure 6a,b. Note that for layout B, which was calibrated by imposing the K_s, t_c and n_{Mann} values obtained in layout A, the difference between the observed and calculated discharge is worse than that of layout A, as would be expected, because these parameters were not recalibrated. Furthermore, Figure 6a shows that contrarily to the experimental runs that achieved the

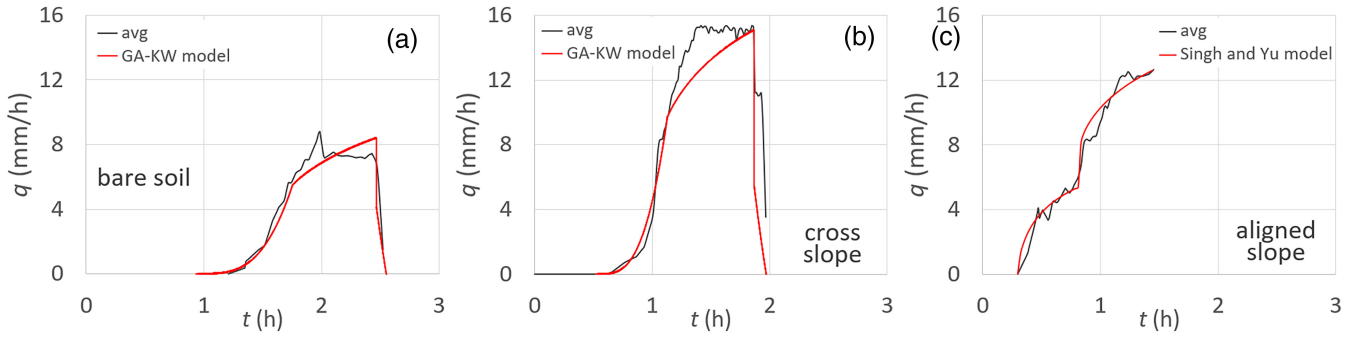

FIGURE 6 Comparison between the temporal variations of the average specific discharge measurements (avg) with those obtained by models' calibration corresponding to (a) layout A (bare soil), (b) layout B (cross slope panels), and (c) layout C (aligned slope panels) (Figure 1).

TABLE 2 Output parameters corresponding to Layouts A and B.

Layout	Model	t_p (h)	ω (h)	t_k (h)	f_k (mm/h)	h_k (mm)	q_k (mm/h)	$f(t_r)$ (mm/h)	$h(t_r)$ (mm)	$q(t_r)$ (mm/h)
(A) bare soil	GA-KW	0.932	19.0	1.754	47.35	3.33	5.48	45.19	4.13	8.41
(B) cross slope panels		0.524		1.130	50.53	4.43	9.70	46.55	5.53	15.09

TABLE 3 Input parameters corresponding to Layout C.

Layout	Model	Panel	i (mm/h)	T_a (h)	t_r (h)	K (mm/h^A)	A	L (m)	n_{Mann} (s m$^{-1/3}$)	S_0 (%)
(C) aligned slope panels	Singh and Yu (1987)	DS	56	**0.300**	1.442	**124.21**	**0.758**	0.7	0.909	0.14
		US		**0.817**		**41.21**		2.2		

Note: Bold values indicate calibrated parameters.

equilibrium condition, for the GA-KW model the outlet discharge increases in the 2nd kinematic domain, and the equilibrium is not reached. The latter could be ascribed to the formation of a soil seal that actually reduces the soil permeability providing the equilibrium and to the fact that the physical model does not account for such a process. It is expected that the seal formation could be more relevant when panels are applied (see Figure 6b), since the greater energy of the water application rate concentrated at the panel outlet could favour splash erosion (van Dijk et al., 2002). The latter mobilizes more soil particles than the direct impact of rainfall. Once deposited later because of overland flow, these may also contribute to decreasing permeability along the path (Slattery & Bryan, 1994).

For layouts A and B, the output parameters corresponding to the application of GA-KW model t_p (Equation (1)), ω (Equation (2)), t_k (Equation (5a)), f_k (Equation (5b)), the water depth at the kinematic arrival time h_k, (Baiamonte & Agnese, 2010) and the corresponding specific discharge q_k, the infiltration capacity at the rainfall duration $f(t_r)$, and the corresponding water depth and discharge, $h(t_r)$ and $q(t_r)$, are all reported in Table 2.

For layout C and for the two aligned slope panels (DS and US), Table 3 reports the input parameters required by the border irrigation model (Singh & Yu, 1987). In particular, for each panel, Table 3 reports the rainfall intensity i, Kostyakov's infiltration parameters, K and A, the time of the advance phase T_a, the duration of the rain, t_r, the length L of each aligned slope panel (Figure 1c), Manning's roughness factor, n_{Mann} and the slope of the plot, S_0.

Note that i, n_{Mann} and S_0 are the same values established for layouts A and B. In other words, the remaining time T_a, K, and A were considered as calibrated parameters. This is because the Singh and Yu model accounts for the Kostiakov infiltration model, rather than the GA model, with new parameters to be calibrated. By fitting the Singh and Yu model to the experimental measurements, only the advance phase, T_a, was expected to be changed for the US and DS panels, because of the different distance from the outlet. Contrarily, fit also became necessary to diversify the scale parameter K associated with the US and DS panels, to obtain reasonable results.

Specifically, minimizing the mean square errors between the measured and estimated specific discharges, $A = 0.758$, for both panels, and K_{DS} and K_{US} resulted in values of 124.21 and 41.21 mm/h^A for DS and US panels, respectively (Table 3).

This issue might appear meaningless because the initial soil characteristics are the same downstream of the two panels. However, it could be justified, by considering that, contrary to layouts A and B where a uniform water application rate was applied, for layout C, the runoff generated by the US panel overflows on the soil that was already wetted by the DS panel. It is reasonable to suppose that this occurrence determines a reduction in soil permeability to be associated with the US panel, which is in line with the calibrated K values. These considerations are supported by the work of Zimmermann et al. (2013), who studied two sampling approaches so as to adequately characterize K_s spatial variability along flowlines. These authors found that in the lower parts of flowlines, soil permeability

TABLE 4 Output parameters corresponding to Layouts C).

Layout	Model	Panel	h_e (mm)	$q(t_r)$ (mm/h)	$Q(t_r)$ (L/h)	$\Sigma Q(t_r)$ (L/h)
(C) aligned slope panels	Singh and Yu (1987)	DS	1.204	13.46	20.19	37.75
		US	1.107	5.85	17.56	

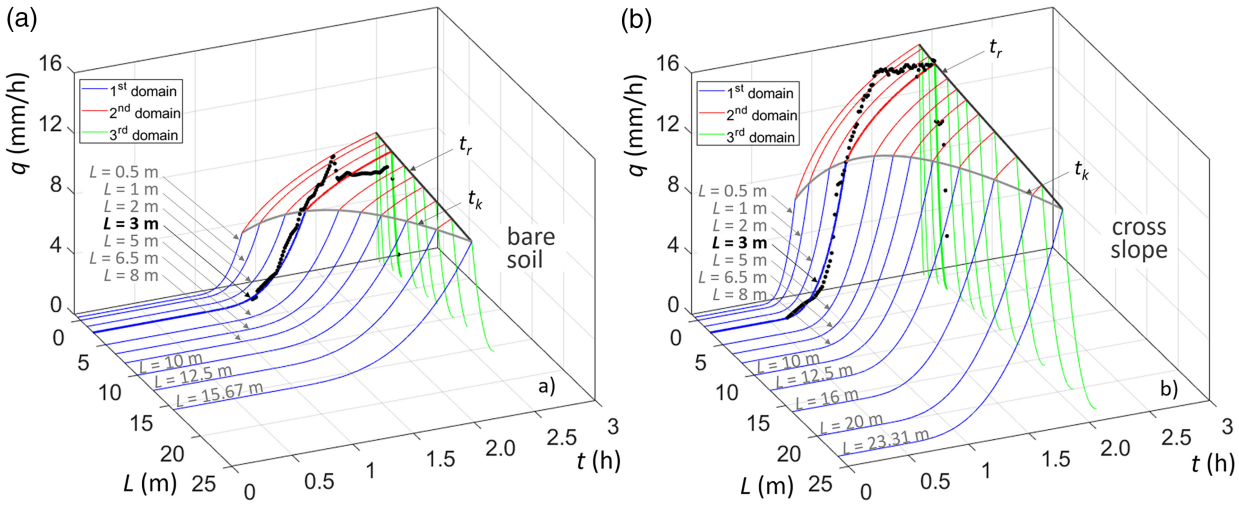

FIGURE 7 Temporal variation of the specific discharge, q (mm/h), obtained by upscaling the Green-Ampt Kinematic-Wave model (GA-KW, Baiamonte & Agnese, 2010) calibrated for $L = 3$ m to different L, (a) for layout A, and (b) for layout B.

decreased, since flowlines had been subject to topsoil removal due to steady erosion by overland flow.

Moreover, it is not farfetched to suppose that the overland flow generated by the DS panel, determines the development of compaction and sealing that also contribute to a decrease in surface permeability (Römkens et al., 1985; Yair & Lavee, 1985). Indeed, sedimentational seals developed during overland flow, and afterflow seals consisting of deposited fine clay particles, may also contribute to decreasing permeability along the path (Slattery & Bryan, 1994).

For layout C, the calibration of the Singh and Yu model provided an excellent fitting of the experimental measurements, as depicted in Figure 6c. In the same figure, as for the experimental discharges, a drop in discharge determined by aligned slope panels can be observed, showing the time in which the contribution of the US panel reaches the outlet, adding to that of the DS panel.

For both DS and US panels, the output parameters corresponding to the application of the Singh and Yu model, the water depth at the end of the plot h_e, the specific discharge at the end of the rainfall, $q(t_r)$, and the volumetric discharge of each panel, $Q(t_r)$, and the cumulated one $\Sigma Q(t_r)$, are reported in Table 4.

4 | UPSCALING AND DISCUSSION

The results obtained through the calibration of both the GA-KW model (layouts A and B) and the Singh and Yu model (layouts C) allows these same models, calibrated for the hillslope 3 m length, to be upscaled to different Ls. This issue is of interest since the actual impact of solar farms or PV systems involves a multitude of panels that could exasperate the increase of the peak discharge that this present work has analysed at a small scale (3 m × 1 m, Figure 1).

For layouts A and B, Figure 7a,b illustrate the 3D plots, respectively, where the rising limb of the hydrograph is represented for different L. The rainfall intensity and the duration of rainfall was set equal to that considered in the experimental runs, $i = 56$ mm/h and, $t_r = 2.47$ and 1.87 h, for layouts A and B, respectively. Of course, the kinematic arrival time, t_k, increased as the hillslope length increased, which was varied until the duration of rainfall ($t_k = t_r$) was achieved, resulting in $L = 15.67$ m for layout A, and $L = 23.31$ m for layout B.

As expected, increasing the length of the hillslope determined a slower response in terms of specific discharge. A comparison between Figure 7a,b also shows that for a fixed upscaled length, the specific discharges when panels are cross slope with respect to the hillslope is greater than those of bare soil, clearly demonstrating their impact on surface runoff.

It is also important to consider that the effect of the length, L, on the hillslope response, for fixed slope, reflects the effect of the slope, S_0, for fixed hillslope length, because the effect of both L and S_0 is lumped (consolidated) in the k_* parameter (Equation 3). For the calibrated n_{Mann} value (0.909 s m$^{-1/3}$), Table 5 reports the k_* values calculated by Equation (3), for fixed slope ($S_0 = 14\%$) by varying the length L (Figure 7a,b), and for fixed length ($L = 3$ m) by varying the slope S_0. Table 5 shows that to any pair (L, S_0) corresponds the same k_* value, indicating that for fixed $L = 3$ m, Figure 7a,b also show the effect of the S_0 values reported in Table 5.

TABLE 5 For the calibrated $n_{Mann} = 0.909$ s m$^{-1/3}$, values of k_* (Equation (3)) corresponding to the upscaled L, for fixed $S_0 = 14$ %, and corresponding to the upscaled S_0, for fixed $L = 3$ m.

L (m) ($S_0 = 14$ %)	k_* Equation (3)	S_0 ($L = 3$ m)
0.5	2.964	5.0400
1	1.482	1.2600
2	0.741	0.3150
3	0.494	0.1400
5	0.296	0.0504
6.5	0.228	0.0298
8	0.185	0.0197
10	0.148	0.0126
12.5	0.119	0.0081
16	0.093	0.0049
20	0.074	0.0031
23.31	0.064	0.0023

The results of upscaling obtained for layouts A and B are reported in Table 6, which shows that as L increases, values of the kinematic arrival time, t_k, and of the corresponding specific discharge, also increase. Contrarily, for layouts A and B, the specific discharge at the end of the rainfall, $q(t_r)$ decreases, but it results in higher outlet discharges, that is, when expressing Q in (L/h).

For layout C, upscaling the Singh and Yu model to different L, required extrapolating the empirical Kostyakov's infiltration parameter, K, based on the calibration results (Table 3), whereas the shape factor A was assumed as a constant for any L.

In the hydrologic literature, the temporal and spatial variation of the saturated hydraulic conductivity, K_s, which is related to the K parameter (Su et al., 2016), has often been described by a power-law. Beven (1982) used the simple piston displacement model to simulate flow in the unsaturated zone, adopting a power-law to describe K_s decreasing as soil depth increases (Baiamonte & Agnese, 2016). Akgün (2010) studied the compaction permeameter tests on mixtures ranging from 15% to 30% bentonite content and showed that the hydraulic conductivity decreased with increased bentonite content, also obeying a power-law. Contrarily, a decaying exponential-law was employed for K_s by Baiamonte et al. (2019) to describe how K_s decreases due to the subsidence phenomena of *Posidonia oceanica* (L.) Delile residues, exposed to a constant rainfall intensity.

The most widely used approach of interest for this work relates saturated permeability to porosity via a power-law (Guarracino et al., 2014), which can also be derived from the Kozeny (1927) and Carman (1937) infiltration models. Since the reduction of Kostyakov's infiltration parameter K was ascribed to sedimentational seals developed during overland flow, and thus is also related to a reduction in soil porosity, the simple decaying power-law was also applied in the context of this work, to extrapolate the decreasing K parameter. The model's calibration provided only two K values, since only two aligned slope panels were installed to perform the experimental runs. A decreasing potential power-law was assumed for extrapolating K to more than two panels, that is, at increasing L (Figure 1c).

Figure 8 plots the power-law applied to Kostyakov's empirical parameters, K (mm/h^A), which were obtained by the calibration of the Singh and Yu model, versus the length L (m). Figure 8 also shows the K values extrapolated by the power-law for three and four panels (red dots), under the assumption of the same interspace panels adopted in the experimental runs (0.7 m). The resulting K values are also reported in Table 6, together with the T_a and h_e parameters, and the output discharges were obtained by upscaling the Singh and Yu model to different L values (Figure 1c).

The corresponding hydrographs are plotted in Figure 9, in terms of specific discharge, q (mm/h) (Figure 9a) and outlet discharge (Figure 9b). Figure 9b also graphs the cumulated discharge, ΣQ, which results from the combined contributions flowing out from the panels, under the assumption of validity of the superposition principle.

Results clearly show that for the aligned slope panels, the outlet discharge is greater than that of the bare soil (no panels), demonstrating the impact of solar panels on overland flow generation. This is also true for layout C.

Finally, for a homogeneous comparison of discharge, by fixing the hillslope length at 3 m and the duration of rainfall at $t_r = 1.44$ h, which corresponds to the rainfall's duration for layout C, the generated outlet discharge was analysed for the case with no panels and the cases with panels. In particular, the ratio between the resulting outlet discharge for layouts A–C, Q_A, Q_B and ΣQ_C, respectively, were estimated by the models. The outlet discharge of layouts B and C compared to layout A (no panels) were found to be 11.7 and 11.5 times greater than that obtained for bare soils, clearly indicating (i) the important effect of the panels providing discharges that are much greater than that corresponding to bare soil, and (ii) that the panels' orientation slightly affects the outlet discharge, since for both of the studied orientation, the discharge ratios are similar to each other.

According to the results obtained by upscaling the models, longer hillslopes further increased outlet discharges, as well as time to runoff, with the exception of aligned slope panels where the same parameters did not vary with the hillslope length.

These results, although predictable and based on simplified assumptions, quantify the effect of solar panels on runoff generation and suggest that erosion control methods should be used to mitigate soil detachment and transportation. Thus, a grass cover beneath the panels and in the interspace between panels (for aligned slope panels) is highly recommended, because the soil appears much more prone to erosion generated by the higher discharges produced when solar panel systems are adopted.

5 | CONCLUSIONS

Solar farms are the energy generators of the future; thus, it is important to determine the environmental and hydrologic effects of both existing and planned farms. This is even more true because

TABLE 6 Results obtained by upscaling the models calibrated for $L = 3$ m to different L.

Layout	Model	L (m)	t_k (h)	t_r (h)	K_s (mm/h)	t_c (h)	$q(t_k)$ (mm/h)	$q(t_k)$ (L/h)	$q(t_r)$ (mm/h)	$q(t_r)$ (L/h)
(A) bare soil	Green Ampt and Kinematic Wave (Baiamonte & Agnese, 2010)	0.5	1.361	2.467	39.2	0.484	3.603	1.80	8.659	4.33
		1	1.483				4.275	4.27	8.592	8.59
		2	1.640				5.019	10.04	8.491	16.98
		3	**1.754**				**5.483**	**16.45**	**8.408**	**25.22**
		5	1.926				6.095	30.48	8.264	41.32
		6.5	2.029				6.418	41.71	8.166	53.08
		8	2.119				6.676	53.41	8.070	64.56
		10	2.224				6.959	69.59	7.943	79.43
		12.5	2.339				7.241	90.51	7.779	97.24
		15.67	2.467				7.531	118.00	7.532	118.02

Layout	Model	L (m)	t_k (h)	t_r (h)	K_s (mm/h)	t_r (h)	$q(t_k)$ (mm/h)	$q(t_k)$ (L/h)	$q(t_r)$ (mm/h)	$q(t_r)$ (L/h)
(B) cross panels	Green Ampt and Kinematic Wave (Baiamonte & Agnese, 2010)	0.5	0.837	1.867	39.2	0.484	6.588	3.29	15.374	7.69
		1	0.927				7.717	7.72	15.297	15.30
		2	1.044				8.945	17.89	15.182	30.36
		3	**1.130**				**9.696**	**29.09**	**15.089**	**45.27**
		5	1.259				10.664	53.32	14.929	74.65
		6.5	1.337				11.171	72.61	14.823	96.35
		8	1.405				11.576	92.61	14.721	117.77
		10	1.485				12.008	120.08	14.591	145.91
		12.5	1.573				12.442	155.53	14.432	180.40
		16	1.680				12.920	206.72	14.206	227.30
		20	1.787				13.349	266.98	13.928	278.56
		23.306	1.866				13.642	317.94	13.645	318.01

Layout	Model	L (m)	T_a (h)	t_r (h)	K (mm/h^A)	A	h_e (mm)	q (t_r) (mm/h)	Q (t_r) (L/h)	$\Sigma Q(t_r)$ (L/h)
(C) aligned slope panels	Singh and Yu (1987)	0.7	0.300	2.694	124.21	0.758	1.325	15.79	23.69	23.69
		2.2	**0.817**		**41.21**		**1.276**	**15.32**	**22.25**	**45.95**
		3.7	1.333		24.97		1.238	14.91	21.14	67.09
		5.2	1.850		17.99		1.194	14.50	19.90	86.99

Note: Bold values refer to the hillslope lengths for which the models were calibrated.

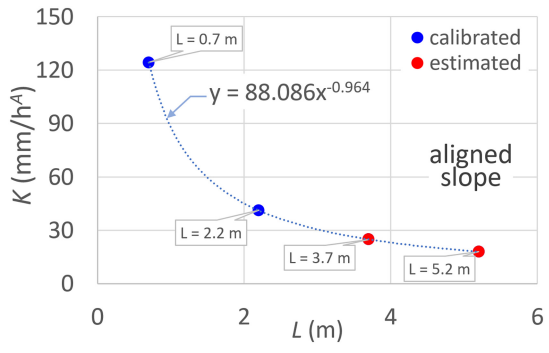

FIGURE 8 For layout C (aligned slope panels), Kostyakov's infiltration empirical parameter, K (mm/h^A), versus the length L (m) (Figure 1c). Red dots indicate the K values estimated by the power law relationship, also indicated.

agrophotovoltaic systems (solar farms) seem to be the most sustainable tool to create renewable energy without compromising agricultural production. In this context, a multidisciplinary approach to study the impact of these kinds of systems becomes more and more important, especially regarding the identification of the most suitable areas for their construction.

In this article, the impact of solar panels on the runoff generation process was investigated from both an experimental and theoretical point of view. The different arrangement of solar panels with respect to the maximum slope direction of the hillslope where the panels are placed was also analysed. Physical models introduced in the literature helped explain the impact of solar panels on runoff generation. The models were calibrated for the experimental layouts and were then upscaled to different hillslope length values.

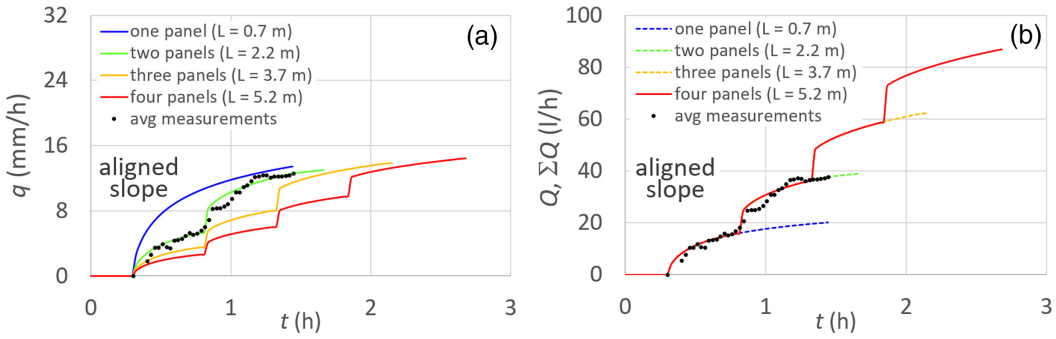

FIGURE 9 For layout C (aligned slope panels), temporal variation (a) of the specific discharge, q (mm/h), and (b) of the outlet discharge for 1–4 panels, Q (L/h) and cumulated, ΣQ (L/h), obtained by upscaling to different L the Singh and Yu model (Singh & Yu, 1987) that was calibrated for $L = 2.2$ m.

Results showed that solar panels increased the outlet discharge when panels were arranged in a cross slope (layout B) and aligned slope (layout C), by 11.7 and 11.5 times, respectively, compared to bare soil (layout A—no panels). This clearly indicates (i) the important effect of the panels on discharges that are much greater than those occurring on bare soil, and (ii) that the panels' orientation slightly affects the outlet discharge, since for both of the studied orientations, the discharge ratios were similar to each other.

Furthermore, solar panels also affected the time to runoff, which was observed to be the lowest for aligned slope panels (0.3 h), higher for cross slope panels (0.62 h), and the highest for the bare soil hillslope (1.2 h). The calibrated theoretical models estimated times to runoff that were very close to those observed.

As it would be expected, upscaling the models to longer hillslope further increased the simulated outlet discharge values, as well as the time to runoff, with an exception for aligned slope panels where time to runoff did not vary with the hillslope length.

The evidence provided by this research suggests that agricultural soils should preferentially not be left bare under solar panel structures, because of an increased risk of runoff and of the relative soil erosion process.

DATA AVAILABILITY STATEMENT

The data that support the findings of this study are available from the corresponding author upon reasonable request.

ORCID

Giorgio Baiamonte https://orcid.org/0000-0002-7092-1177

REFERENCES

Abrahams, A. D., & Parsons, A. J. (1994). Hydraulics of interrill overland flow on stone-covered desert surfaces. *Catena*, *23*, 111–140.

Akgün, H. (2010). Geotechnical characterization and performance assessment of bentonite/sand mixtures for underground waste repository sealing. *Applied Clay Science*, *49*(4), 394–399. Conference Paper.

Atchison, K. T. (1973). Retardance coefficient and other data for a vegetated irrigation border. Unpublished M.S. Thesis, University of Arizona, Tucson, AZ, USA.

Baiamonte, G. (2016). Simplified model to predict runoff generation time for well-drained and vegetated soils. *Journal of Irrigation and Drainage Engineering-ASCE*, *142*(11), 04016047. https://doi.org/10.1061/(ASCE)IR.1943-4774.0001072

Baiamonte, G., & Agnese, C. (2010). An analytical solution of kinematic wave equations for overland flow under Green-Ampt infiltration. *Journal of Agricultural Engineering*, *1*, 41–49. http://agroengineering.org/index.php/jae/article/view/jae.2010.1.41

Baiamonte, G., & Agnese, C. (2016). Quick and slow components of the hydrologic response at the hillslope scale. *Journal of Irrigation and Drainage Engineering-ASCE*, *142*(10), 4016038. https://doi.org/10.1061/(ASCE)IR.1943-4774.0001053

Baiamonte, G., D'Asaro, F., & Calvo, R. (2019). Gravity-driven infiltration and subsidence phenomena in *Posidonia oceanica* residues. *Journal of Hydrologic Engineering ASCE*, *24*(6), 4019016. doi:10.1061/(ASCE)HE.1943-5584.0001791

Baiamonte, G., D'Asaro, F., & Grillone, G. (2014). Simplified probabilistic-topologic model for reproducing hillslope rill network surface runoff. *Journal of Irrigation and Drainage Engineering-ASCE*, *141*(7), 4014080. https://doi.org/10.1061/(ASCE)IR.1943-4774.0000854

Baiamonte, G., & Singh, V. P. (2016). Analytical solutions of kinematic wave time of concentration for overland flow under Green-Ampt infiltration. *Journal of Hydrologic Engineering ASCE*, *21*(3), 4015072. https://doi.org/10.1061/(ASCE)HE.1943-5584.0001266

Beven, K. J. (1982). On subsurface stormflow: Predictions with simple kinematic theory for saturated and unsaturated flows. *Water Resources Research*, *18*(6), 1627–1633.

Bignami, D. (2010). E i pannelli colonizzano i campi. *Terra e Vita*, *43*, 16 (in italian).

Brutsaert, W. (2005). *Hydrology: An introduction*. Cambridge University Press.

Carman, P. C. (1937). Fluid flow through granular beds. *Transactions. Institute of Chemical Engineers*, *15*, 150–166.

Caviedes-Voullième, D., Ahmadinia, E., & Hinz, C. (2021). Interactions of microtopography, slope and infiltration cause complex rainfall-runoff behavior at the hillslope scale for single rainfall events. *Water Resources Research*, *57*, e2020WR028127. https://doi.org/10.1029/2020WR028127

Choi, C. S., Cagle, A. E., Macknick, J., Bloom, D. E., Caplan, J. S., & Ravi, S. (2020). Effects of revegetation on soil physical and chemical properties in solar photovoltaic infrastructure. *Frontiers in Environmental Science*, *8*, 1–9. https://doi.org/10.3389/fenvs.2020.00140

Cook, L. M., & McCuen, R. H. (2013). Hydrologic response of solar farms. *Journal of Hydrologic Engineering, ASCE*, *18*(5), 536–541. https://doi.org/10.1061/(ASCE)HE.1943-5584.0000530

Courant, R., & Hilbert, D. (1962). *Methods of Mathematical Physics*, vol. 2, Wiley-Interscience.

Dupraz, C., Marrou, H., Talbot, G., Dufour, L., Nogier, A., & Ferard, Y. (2011). Combining solar photovoltaic panels and food crops for optimising land use: Towards new agrivoltaic schemes. *Renewable energy*, *36*, 2725–2732.

Elamri, Y., Cheviron, B., Mange, A., Dejean, C., Liron, F., & Belaud, G. (2018). Rain concentration and sheltering effect of solar panels on cultivated plots. *Hydrology and Earth System Sciences*, *22*, 1285–1298. https://doi.org/10.5194/hess-22-1285-2018

Giráldez, J. V., & Woolhiser, D. A. (1996). Analytical integration of the kinematic equation for runoff on a plane under constant rainfall rate and smith and Parlange infiltration. *Water Resources Research*, *32*(11), 3385–3389.

Green, W. H., & Ampt, G. A. (1911). Studies of soil physics, I, flow of air and water through soils. *The Journal of Agricultural Science*, *4*, 1–24.

Guarracino, L., Rötting, T., & Carrera, J. (2014). A fractal model to describe the evolution of multiphase flow properties during mineral dissolution. *Advances in Water Resources*, *67*, 78–86. https://doi.org/10.1016/j.advwatres.2014.02.011

Hernandez, R. R., Easter, S. B., Murphy-Mariscal, M. L., Maestre, F. T., Tavassoli, M., Allen, E. B., Barrows, C. W., Belnap, J., Ochoa-Hueso, R., Ravi, S., & Allen, M. F. (2014). Environmental impacts of utility-scale solar energy. *Renewable and Sustainable Energy Reviews*, *29*, 766–779. https://doi.org/10.1016/j.rser.2013.08.041

IPCC, Intergovernmental Panel on Climate Change. (2014). Climate change: Impacts, adaptation, and vulnerability. Part A: Global and sectoral aspects. In C. B. Field, et al. (Eds.), *Contribution of Working Group II to the Fifth Assessment Report of the Intergovernmental Panel on Climate Change*. Cambridge Univ Press.

IRENA. (2019). Future of solar photovoltaic: Deployment, investment, technology, grid integration and socio-economic aspects (A global energy transformation: paper), International Renewable Energy Agency, Abu Dhabi.

Kincaid, D. C., Solomon, K. H., & Oliphant, J. C. (1996). Dropsize distribution for irrigation sprinklers. *Transactions of the American Society of Agricultural Engineers*, *39*(3), 839–845.

Kohl, R. A. (1974). Drop size distribution from a medium sized agricultural sprinkler. *Transactions of the American Society of Agricultural Engineers*, *17*(5), 690–693.

Kostyakov, A. N. (1932). On the dynamics of the coefficient of water percolation in soils and on the necessity of studying it from a dynamic point of view for purpose of amelioration. Trans Sixth Committee International Soc Soil Sci, Part A, Russian, pp. 17–21.

Kozeny, J. (1927). Über kapillare leitung des wassers im boden. *Sitzungsber Akad Wiss*, *136*, 271–306.

Lambert, Q., Bischoff, A., Cueff, S., Cluchier, A., & Gros, R. (2021). Effects of solar park construction and solar panels on soil quality, microclimate, CO_2 effluxes, and vegetation under a Mediterranean climate. *Land Degradation Development*, *32*(18), 5190–5202. https://doi.org/10.1002/ldr.4101

Lawrence, D. S. L. (1997). Macroscale surface roughness and frictional resistance in overland flow. *Earth Surface Processes and Landforms*, *22*, 365–382.

McDonnell, J. J., Spence, C., Karran, D. J., van Meerveld, H. J., & Harman, C. J. (2021). Fill-and-spill: A process description of runoff generation at the scale of the beholder. *Water Resources Research*, *57*, e2020WR027514. https://doi.org/10.1029/2020WR027514

PNIEC. (2023). Integrated National Energy and Climate Plan. https://commission.europa.eu/energy-climate-change-environment/implementation-eu-countries/energy-and-climate-governance-and-reporting/national-energy-and-climate-plans_en

Roels, J. M. (1984). Flow resistance in concentrated overland flow on rough slope surfaces. *Earth Surface Processes and Landforms*, *9*, 541–551.

Römkens, M. J. M., Baumhardt, R. L., Parlange, M. B., Parlange, J.-Y., Whisler, F. D., & Prasad, S. N. (1985). Effect of rainfall characteristics on seal hydraulic conductance. In F. Callebaur, D. Grabriels, & M. DeBoodt (Eds.), *Proceedings of International Symposium on the Assessment of Soil Surface and Crusting* (pp. 228–235). Flanders Research Center for Soil Erosion and Soil Conservation.

Roth, R. L. (1971). Roughness during border irrigation. [Masters dissertation, Univ. of Arizona, Tucson, AZ, USA].

Singh, V. P., & Su, Q. (2022). Irrigation engineering. In *Principles, processes, procedures, design, and management*. University Press.

Singh, V. P., & Yu, F. X. (1987). A mathematical model for border irrigation I. Advance and storage phases. *Irrigation Science*, *8*, 151–174.

Slattery, M. C., & Bryan, R. B. (1994). Surface seal development under simulated rainfall on an actively eroding surface. *Catena*, *22*(1), 17–34. https://doi.org/10.1016/0341-8162(94)90063-9

Su, L., Wang, Q., Shan, Y., & Zhou, B. (2016). Estimating soil saturated hydraulic conductivity using the Kostiakov and Philip infiltration equations. *Soil Science Society of America Journal*, *80*, 1463–1475. https://doi.org/10.2136/sssaj2016.04.0125

van Dijk, A. I. J. M., Bruijnzeel, L. A., & Rosewell, C. J. (2002). Rainfall intensity–kinetic energy relationships: A critical literature appraisal. *Journal of Hydrology*, *261*, 1–23.

Wang, F., & Gao, J. (2023). How a photovoltaic panel impacts rainfall-runoff and soil erosion processes on slopes at the plot scale. *Journal of Hydrology*, *620*, 129522.

Woolhiser, D. A., & Liggett, J. V. (1967). Unsteady, one-dimensional flow over a plane—The rising hydrograph. *Water Resources Research*, *3*(3), 753–771.

Wu, C., Liu, H., Yu, Y., Zhao, W., Liu, J., Yu, H., & Yetemen, O. (2022). Eco-hydrological effects of photovoltaic solar farms on soil microclimates and moisture regimes in arid Northwest China: A modeling study. *Science of the Total Environment*, *802*, 149946. https://doi.org/10.1016/j.scitotenv.2021.149946

Yair, A., & Lavee, H. (1985). Runoff generation in arid and semi-arid zones. In M. G. Anderson & T. P. Burt (Eds.), *Hydrological forecasting* (pp. 183–220). Wiley.

Zainol Abidin, M. A., Mahyuddin, M. N., & Mohd Zainuri, M. A. A. (2021). Solar photovoltaic architecture and agronomic management in agrivoltaic system: A review. *Sustainability*, *13*(14), 7846. https://doi.org/10.3390/su13147846

Zimmermann, A., Schinn, D. S., Francke, T., Elsenbeer, H., & Zimmermann, B. (2013). Uncovering patterns of near-surface saturated hydraulic conductivity in an overland flow-controlled landscape. *Geoderma*, *195–196*, 1–11.

How to cite this article: Baiamonte, G., Gristina, L., & Palermo, S. (2023). Impact of solar panels on runoff generation process. *Hydrological Processes*, *37*(12), e15053. https://doi.org/10.1002/hyp.15053

APPENDIX A: The GA-KW model

The Green-Ampt Kinematic wave model (GA-KW) model deals with the analytical solution of kinematic wave equations for overland flow occurring in a hillslope where the infiltration process is governed by the Green-Ampt model (Baiamonte & Agnese, 2010). The kinematic wave equations can be derived by the so-called shallow water equations (Brutsaert, 2005), expressing the conservation of mass and momentum, respectively:

$$\frac{\partial h}{\partial t}+L\frac{\partial q}{\partial x}=(i-f), \tag{A1}$$

$$\frac{\partial u}{\partial t}+u\frac{\partial u}{\partial x}+g\frac{\partial h}{\partial x}=g(S_0-S_f)-\frac{u}{h}(i-f), \tag{A2}$$

where h is the mean depth of flow, t is the time, L is the hillslope length, q is the specific discharge, x is the downslope distance from the top of the hillslope, i is the rainfall intensity, f is the infiltration capacity, u is the flow velocity, g is the acceleration due to gravity, S_0 is the bed slope, and S_f is the friction slope. Under the assumption that the inertia and diffusion effects are negligible with respect to that of gravity and of friction, Equation (A2) simply reduces to $S_f = S_0$. Physically, this equivalence states that the friction slope is assumed to be equal to the bed slope, therefore the Manning equation can be written as a function of S_0:

$$q=\left(\frac{\sqrt{S_0}}{n_{\text{Mann}}L}\right)h^m=k_*h^m, \tag{A3}$$

where n_{Mann} is the Manning friction factor, m accounts for the flow regime (m is usually taken to be equal to 5/3 for turbulent flow, to 2 for transitional flow and to 3 for laminar flow) and the k_* parameter (in brackets) consolidates the hillslope 'geometry' (length, slope and roughness).

By assuming the common initial and boundary conditions of null water depth $h(0, t) = h(x, 0) = 0$, Equations (A1) and (A3) lead to:

$$\frac{\partial h}{\partial t}+m\,k_*L\,h^{m-1}\frac{\partial h}{\partial x}=(i-f). \tag{A4}$$

Equation (A4) describes the kinematic wave approximation and can be solved by the method of characteristics (Courant & Hilbert, 1962), which converts Equation (A4) to a pair of ordinary differential equations, expressing the time variation of water depth:

$$\frac{dh}{dt}=r(t)=i-f(t), \tag{A5}$$

and the characteristic curve:

$$\frac{dx}{dt}=L\frac{dq}{dh}=m\,k_*\,L\,h^{m-1}=m\,u. \tag{A6}$$

The unique relationship between q and h, expressed by (A3), together with (A5) and (A6) allows to state that an imaginary observer moving in $x - t$ plane at a speed equal to the kinematic wave celerity would see the flow rate increases at a rate equal to the lateral inflow ($i - f$). The characteristic curves may be grouped in several domains, recognizable in a $x - t$ plane, depending on their origin: the distance axis at the time to ponding for the first domain, the part of the time axis from t_p up to the duration of rain, t_r, for the second domain, and the rest of $x - t$ plane for the third domain (falling limb).

According to the Green and Ampt model, the infiltration rate $f(t)$ in Equation (A5) is given by:

$$t-t_p=t_c\left(\frac{K_s}{(f-K_s)}-\frac{K_s}{(i-K_s)}+\Psi\right), \tag{A7}$$

where t_p is the time to ponding, t_c is the sorptivity time scale (Equation (2)), K_s is the saturated hydraulic conductivity, and the dimensionless function Ψ is equal to:

$$\Psi=ln\left(\frac{i(f-K_s)}{f(i-K_s)}\right). \tag{A8}$$

By using Equation (A7), the cumulative depth of rainfall excess at any instant t, $h(t)$, was derived (Baiamonte & Agnese, 2010):

$$h(t)=\int_{t_p}^{t}r(t)dt=\int_{t_p}^{t}(i-f(t))dt=t_c\left(\frac{i-f}{f-K_s}K_s+i\,\Psi\right), \tag{A9}$$

where $r(t)$ is the instantaneous rainfall excess. Under the assumption of transitional flow regime ($m = 2$), in the following only the solutions provided by the integration of the kinematic equations in the first two domains (Baiamonte & Agnese, 2010; Giráldez & Woolhiser, 1996) are reported.

***Domain 1: Characteristic originating at* ($0 < x < L$, $t = t_p$)**

For the first domain, at the time to ponding, characteristics, originating at any section distant x_0 from the top of the hillslope, are defined as:

$$\int_{x_0}^{x}dx=m\,k_*L\int_{t_p}^{t}h^{m-1}dt=m\,k_*L\int_0^h\frac{h^{m-1}}{i-f}dh. \tag{A10}$$

Integration of Equation (A10) provided (Baiamonte & Agnese, 2010):

$$\frac{x}{L}=\frac{t_c^2\,k_*}{(f-K_s)^2(i-K_s)}\cdot\Big[(i-f)(f+i-2K_s)K_s^2 + i(i-K_s)(f-K_s)\Psi(2K_s+(f-K_s)\Psi)\Big]. \tag{A11}$$

***Domain 2: Characteristic originating at* ($x = 0$, $t_p < t < t_r$)**

To analytically derive the characteristic curves of the second domain, originating at any time $t_0 > t_p$, it is first necessary to express the water depth h as a function of t_0 (through f_0):

$$h=\int_{t_0}^{t}(i-f)dt=(i-f)(t-t_0)-\int_f^{f_0}(t-t_0)df, \tag{A12}$$

where f_0 is the infiltration capacity at the time t_0. To integrate Equation (A10), Equation (A3) was applied by replacing the pair (t_p, i) with the pair (t_0, f_0), obtaining:

$$h = t_c\left(\frac{K_s(f_0-f)(i-K_s)}{(f-K_s)(f_0-K_s)}+i\Psi_0\right), \tag{A13}$$

where Ψ_0 function is defined by:

$$\Psi_0 = ln\left(\frac{f_0(f-K_s)}{f(f_0-K_s)}\right), \tag{A14}$$

Finally, to derive characteristics in the second domain, Equation (A13) can be used for the integration of Equation (A6), which for $m = 2$, yielded (Baiamonte & Agnese, 2010):

$$\frac{x}{L} = \frac{t_c^2 k_*}{(f-K_s)^2(f_0-K_s)^2}\left((f_0-f)K_s^2\right)\left[2ff_0 - fi + f_0 i - (f+3f_0)K_s + 2K_s^2\right] + 2[f(f_0-i)+f_0(i-K_s)](f-K_s)(f_0-K_s)K_s\Psi_0 + i(f-K_s)^2(f_0-K_s)^2\Psi_0^2. \tag{A15}$$

Solutions in Equations (A11) and (A15), together with Equation (-A3) allow deriving the rising limbs of the hydrographs displayed in Figure 6a,b and in Figure 7a,b, in terms of specific discharges, q (mm/h). The kinematic arrival time t_k, and the corresponding infiltration capacity, f_k, separating the 1st and 2nd domains (Figure 7a,b) are given in dimensionless terms by Equations (5a) and (5b).